Coulomb-driven terahertz-frequency intrinsic current oscillations in a double-barrier tunneling structure

O. Jonasson and I. Knezevic

Coulomb-driven THz-frequency intrinsic current oscillations
in a double-barrier tunneling structure

O. Jonasson[*] and I. Knezevic[†]

University of Wisconsin-Madison, Madison, Wisconsin 53706-1691, USA

(Dated: September 26, 2014)

We investigate time-dependent, room-temperature quantum electronic transport in GaAs/AlGaAs double-barrier tunneling structures (DBTSs). The open-boundary Wigner-Boltzmann transport equation is solved by the stochastic ensemble Monte Carlo technique, coupled with Poisson's equation and including electron scattering with phonons and ionized dopants. We observe well-resolved and persistent THz-frequency current density oscillations in uniformly-doped, *dc*-biased DBTSs at room temperature. We show that the origin of these intrinsic current oscillations is not consistent with previously proposed models, which predicted an oscillation frequency given by the average energy difference between the quasi-bound states localized in the emitter and main quantum wells. Instead, the current oscillations are driven by the long-range Coulomb interactions, with the oscillation frequency determined by the ratio of the charges stored in the emitter and main quantum wells. We discuss the tunability of the frequency by varying the doping density and profile.

PACS numbers: 73.63.-b,73.21.-b,05.60.Gg

I. INTRODUCTION

The THz-frequency range of the electromagnetic spectrum (0.1 – 10 THz) has received considerable attention is recent years[1]. THz-frequency radiation is a valuable tool in the characterization of doped semiconductors, whose typical electron relaxation rates and plasma frequencies are in this range [2,3]. Other uses of THz radiation include non-destructive imaging of samples that are too sensitive for x-rays, opaque at optical and near-infrared frequencies, but transparent to THz-frequency illumination[4,5]. Unfortunately, a lack of compact and efficient sources in this frequency range, referred to as the THz gap, is an impediment to the development and application of THz-based technologies[6].

Semiconductor double-barrier tunneling structures (DBTSs) in which an undoped region, several tens of nanometers wide, envelops the main quantum well and barriers, are usually referred to as resonant-tunneling diodes (RTDs) and can act as a source of power with frequency up to several hundred GHz when biased in the negative differential resistance regime[7]. Recently, RTD oscillators working in the THz-regime have been experimentally realized at room temperature by coupling RTDs with external circuit elements such as slot-antennas[8–11]. However, these experimental systems have low output power, typically in the micro-watt range[8–11], because the oscillations are induced by exchanging energy with external circuit elements[12].

Intrinsic current oscillations in *dc*-biased RTDs were first observed in numerical calculations by Jensen and Buo[13], who found that the oscillations were persistent (did not decay over time). Theoretical work by several other groups predicted the same phenomenon [13–16]. It has been suggested that the RTD intrinsic current oscillations could circumvent the low-power problem and lead to THz-frequency power in the milli-watt range[12]. However, the effect has not yet been observed in experiment.

It is therefore critical to understand the mechanism behind the intrinsic current oscillations, in order to predict the optimal experimental conditions for its observation. Zhao *et al.* [17] proposed a mechanism that emphasized the importance of the formation of a quantum well on the emitter side of the device (the emitter quantum well, EQW) and connected the frequency of the oscillations to the average energy spacing between the bound states in the EQW and the main quantum well (MQW). The work of Jensen and Buo[13] and others [14–16,18,19] on intrinsic current oscillations focused on RTDs with a traditional doping profile (no doping in the region around the well and barriers), where the EQW only forms at low temperature (77 K or below) and in a narrow bias window. For this reason, and due to thermal broadening effects, it has been argued that intrinsic current oscillations could only occur at low temperatures[17].

In this paper, we investigate room-temperature intrinsic current oscillations in GaAs/AlGaAs-based DBTSs under *dc* bias. We show that the intrinsic oscillations stem from long-range Coulomb interactions and are associated with a periodic charge redistribution between the emitter and main quantum wells. The oscillations have the highest amplitude and are closest to single-frequency (harmonic) when the two wells are both deep enough to support well-localized quasibound states close in energy; otherwise, there is a continuum on the emitter side and the oscillations are low in amplitude and have a considerable frequency spread. However, the frequency of the oscillations is not determined by the level spacing between the quasibound states[17], but instead by the amounts of charge stored in the two quantum wells. Considering the Coulomb origin of the oscillations, it is not surprising that a structure different than a traditional RTD is required for observing the oscillations with a high amplitude and sharp frequency. Therefore, instead of the traditionally-doped RTD structures, we focus on *DBTSs with a uniform doping profile*, which

ensures the formation of a deep EQW for all values of applied bias and at room temperature. While the uniformly-doped DBTSs have a low peak-to-valley ratio (a commonly employed figure-of-merit of RTD performance), a wide peak plateau, and would generally perform poorly in traditional RTD applications, they are superior as intrinsic THz-frequency oscillators. We simulate time-dependent room-temperature quantum transport in these systems by solving the Wigner-Boltzmann transport equation (WBTE) by the stochastic ensemble Monte Carlo technique with particle affinities[20,21], coupled self-consistently with Poisson's equation. Scattering is treated microscopically within the WBTE, with rates obtained from time-dependent perturbation theory (Fermi's golden rule)[22]. Our treatment of scattering is more detailed than in earlier work, where scattering was either neglected[23] or was treated using the relaxation-time approximation with a constant (energy-independent) relaxation time [13–15]. We show that the current oscillations are associated with the EQW and MQW ground states being periodically and adiabatically tuned in and out of alignment due to a charge redistribution. The frequency of current oscillations depends linearly on the ratio of the charges stored in the two wells and is lower than the plasma frequency. We discuss the dependence of the current-density-oscillation amplitude (which can be as high as 50–80% of the time-averaged current density), frequency, and bandwidth on the doping density and profile.

This paper is organized into four sections and an appendix. In Sec. II, we present the simulation framework, while Sec. III features the results. We address the intrinsic current oscillations in a uniformly-doped DBTS (Sec. III A) and show a comparison with a comparable traditionally-doped RTD (Sec. III B). We investigate the effects of phonon and ion scattering on the current density in a uniformly-doped DBTS (Sec. III C), provide an explanation for the mechanism behind the current oscillations by employing a quasistatic picture (Sec. III D), show how the doping density affects the device performance as a source of THz ac-current (Sec. III E), and discuss some considerations relevant for potential fabrication of these devices (Sec. III F). We conclude with a summary and final remarks in Sec. IV. In the Appendix, we present our method for treating applied bias when solving the WTBE, which differs from the approaches found in the literature[21,24].

II. SYSTEM AND MODEL DESCRIPTION

The generic structure we consider is a GaAs-based DBTS with two AlGaAs barriers. A schematic of the device is shown in Fig. 1. To simulate the considered system, we solve the open boundary WBTE[21,25,26], which governs the time evolution of the Wigner quasiprobability distribution f_w[27]. We employ the effective-mass approximation (we assume uniform effective mass throughout
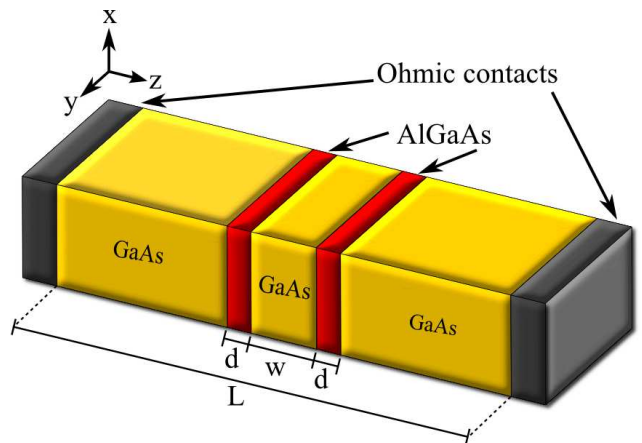

FIG. 1. (Color online) A schematic of the double-barrier GaAs/AlGaAs tunneling structure. The barrier and quantum-well widths are denoted by d and w, respectively, and L is the system length. We assume that the device dimensions in the x and y directions are much greater than its length L.

the structure) with effective mass $m^* = 0.067m_0$, with m_0 being the free-electron rest mass, and assume translational invariance in the $x-y$ plane. The WBTE for quasi-1D transport along z, with k denoting the wave number along z, can be written as[21,26]

$$\frac{\partial f_w}{\partial t} + \frac{\hbar k}{m^*}\frac{\partial f_w}{\partial z} - \frac{1}{\hbar}\frac{\partial V_{cl}}{\partial z}\frac{\partial f_w}{\partial k} = Q_{V_{qm}}[f_w] + C[f_w],$$
(1)

where $Q_{V_{qm}}[f_w]$ is the quantum evolution term defined by

$$Q_{V_{qm}}[f_w](z,k,t) = \int_{-\infty}^{\infty} V_w(z,k-k',t)f_w(z,k',t)\mathrm{d}k',$$
(2)

while $V_w(z,k)$ is the non-local Wigner potential

$$V_w(z,k,t) = \frac{1}{h}\int_{-\infty}^{\infty}\sin(kz')[V_{qm}(z+z'/2,t) - V_{qm}(z-z'/2,t)]\mathrm{d}z'.$$
(3)

Note that in Eqs. (1)-(3), we have assumed that the total potential can be split into a spatially-slowly-varying term $V_{cl}(z,t)$ and a fast-varying term $V_{qm}(z,t)$. It can be shown[21] that potential terms linear or quadratic in position can be included in the slowly-varying term without any approximations, but higher-order terms must be included in the fast-varying term. (In the Appendix, we explain how we perform the separation.)

In Eq. (1), scattering is incorporated via the Boltz-

mann collision operator, defined by

$$C[f_w](z, k, t) = \sum_i \int [s_i(\mathbf{k}', \mathbf{k}) f_w(z, k', t)$$
$$- s_i(\mathbf{k}, \mathbf{k}') f_w(z, k, t)] \mathrm{d}^3 k' , \qquad (4)$$

where $s_i(\mathbf{k}', \mathbf{k})$ is the transition rate from state $\mathbf{k}'$ to $\mathbf{k}$ due to scattering mechanism i. In this work, we consider a GaAs-based device, so the relevant scattering mechanisms are with polar optical phonons and ionized donors[28].

Well-established methods of solving the open-boundary WBTE include the finite-difference approaches[13,14,29] and Monte Carlo methods [20,30–33]. We solve Eq. (1) using a particle-based ensemble Monte Carlo approach, where particles are assigned a property called affinity[20,21]. Quantum effects are accounted for via a time evolution of particle affinities, which are induced by the quantum evolution term in Eq. (1). The method was originally proposed by Shifren and Ferry[20,24,34] and later improved upon by Querlioz and Dollfus[21]. Our approach deviates from that of Querlioz and Dollfus in our treatment of contacts and bias. Here, contacts are assumed to be Ohmic, where charge neutrality and current continuity are enforced by injecting carriers with a velocity-weighted, drifted Maxwell-Boltzmann probability density (Querlioz and Dollfus assumed an equilibrium Maxwell-Boltzmann density[21]) defined by

$$p_L(\mathbf{k}) \propto k \exp \left\{ -\frac{\hbar^2 (k - k_L)^2}{2m^* k_B T} \right\} , k \geq 0 \qquad (5a)$$

$$p_R(\mathbf{k}) \propto |k| \exp \left\{ -\frac{\hbar^2 (k - k_R)^2}{2m^* k_B T} \right\} , k \leq 0 , \qquad (5b)$$

where L (R) refers to the left (right) contact. The drift wave numbers k_L and k_R are drift wave numbers in the left and right contacts, calculated as the expectation values of k on the device side of the contact-device interface,

$$k_{L,R} = \frac{\int_{-\infty}^{\infty} k f_w(z_{L,R}, k, t) \mathrm{d}k}{\int_{-\infty}^{\infty} f_w(z_{L,R}, k, t) \mathrm{d}k} , \qquad (6)$$

where z_L (z_R) is the position of the left (right) contact. The in-plane wave numbers k_x and k_y are generated randomly from a Maxwell-Boltzmann distribution.

Electron–electron interaction is accounted for on a mean-field level, by a self-consistent solution of Poisson's equation. The resulting time-dependent electrostatic potential is included in the V_{qm} term in Eq. (3). Bias is incorporated through the boundary conditions in Poisson's equation (see Appendix).

We calculate the current, I, that would be measured by an external ammeter based on the Shockley-Ramo theorem[35,36], given by Eq. (7a):

$$I(t) = \frac{q}{L} \sum_i A_i v_i \qquad (7a)$$

$$= \frac{qS}{L} \int_{-L/2}^{L/2} \mathrm{d}z \, \langle v \rangle (z, t) n(z, t). \qquad (7b)$$

Here, q is the elementary charge, L is the device length, $v_i = \hbar k_i / m^*$ is the velocity of i-th particle, and A_i is the particle's affinity in the WMC simulation. The above expression (7a) has been widely used in current calculations and is equivalent to tracking the particles that exit/enter each contact, but with less numerical noise because the entire ensemble partakes[21,37,38]. In one dimension, expression (7a) is also proportional to the current density averaged over the device, as captured by Eq. (7b), where S is the device area, $\langle v \rangle (z, t)$ is the average z-component of the electron velocity, and $n(z, t)$ is the electron density.

III. RESULTS

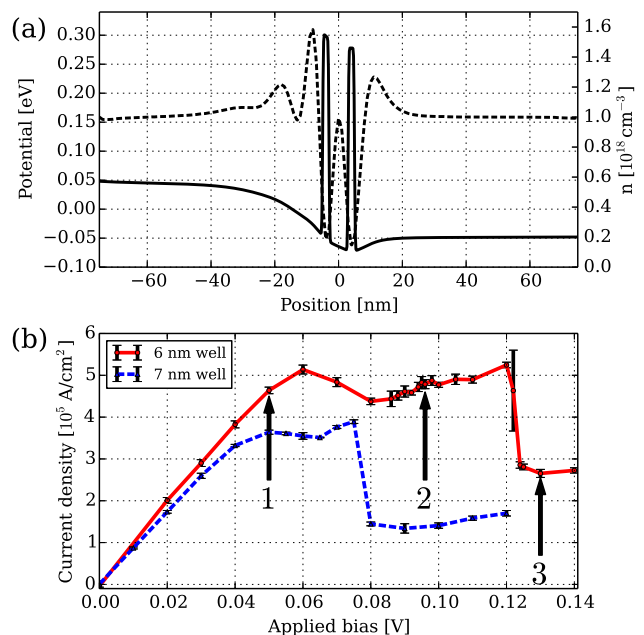### A. DBTS with a uniform doping profile

FIG. 2. (Color online) (a) Time-averaged potential profile (solid) and charge density (dashed) as a function of position for the uniformly-doped DBTS at an applied bias of 96 mV (bias for which intrinsic current oscillations are observed). The potential profile is obtained from a self-consistent solution of the coupled WBTE and Poisson's equation. (b) Time-averaged current density vs applied bias for DBTSs with 6-nm-wide (solid red) and 7-nm-wide (dashed blue) quantum wells. The time average is obtained over 1 ps intervals. Arrows in panel (b) are guides for Fig. 3. Arrow 2 also corresponds to the bias value of 96 mV, which is used in (a).

The device we consider in this section is a 150-nm-long GaAs DBTS with a 6-nm-wide quantum well, sandwiched between two 2-nm-thick $\mathrm{Al}_{0.26}\mathrm{Ga}_{0.74}\mathrm{As}$ barriers with a conduction band offset of 0.35 eV [39] (p. 260). The doping profile is uniform throughout the device, with a density of $10^{18}\mathrm{cm}^{-3}$. The sample potential profile of the 6-nm-well device for an applied bias of 96 mV is shown in Fig. 2a.
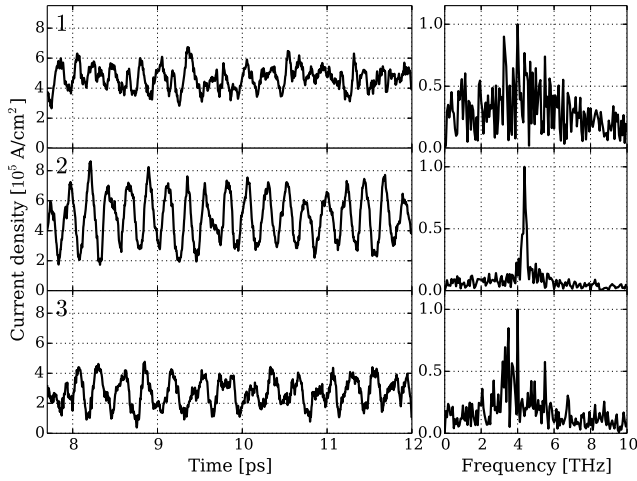
FIG. 3. Current density vs time (left column) and the corresponding Fourier transform amplitudes (right column) for the uniformly-doped DBTS from Sec. III A at an applied bias of 1: 50 mV (top row), 2: 96 mV (middle row) and 3: 130 mV (bottom row). Panel numbers 1-3 refer to the bias values marked in Fig. 2.

Intrinsic oscillations are well-resolved observed in the bias range 94 mV to 98 mV for the 6-nm-well device. In Fig. 2b, two I-V diagrams, one for the 6-nm device and another for a 7-nm-well but otherwise identical device are shown. Arrow 2 in Fig. 2b points to 96 mV, the bias value from Fig. 2a. In contrast to the 6-nm device, no intrinsic oscillations are observed at any bias for the 7-nm-well device.

Figure 3 shows the current density vs time for the three values of applied bias denoted in Fig. 2b, along with the corresponding Fourier transform amplitudes of the current density. We see that the current density fluctuates over time for all considered bias values. However, only for bias values in the range 94 mV to 98 mV do the fluctuations have a well-resolved frequency (i.e. a narrow peak in the frequency domain, middle right panel). The current oscillations do not diminish when the number of particles in the simulation is increased, eliminating the possibility that the current oscillations are artifacts of the stochastic nature of the Monte Carlo method.

B. Traditionally-doped RTD

For comparison, we have considered a traditionally-doped RTD with a 30-nm-wide undoped region that includes the center of the device. Figure 4a shows the potential profile, charge density and doping profile for an applied bias of 180 mV (see Fig. 4b for IV-diagram). The main quantum well is 7-nm-wide (this well width provided the most pronounced current oscillations), with other parameters the same as the uniformly-doped structure considered in Fig. 2. As in the case of the uniformly-doped DBTS considered in Sec. III A, we observe persis-
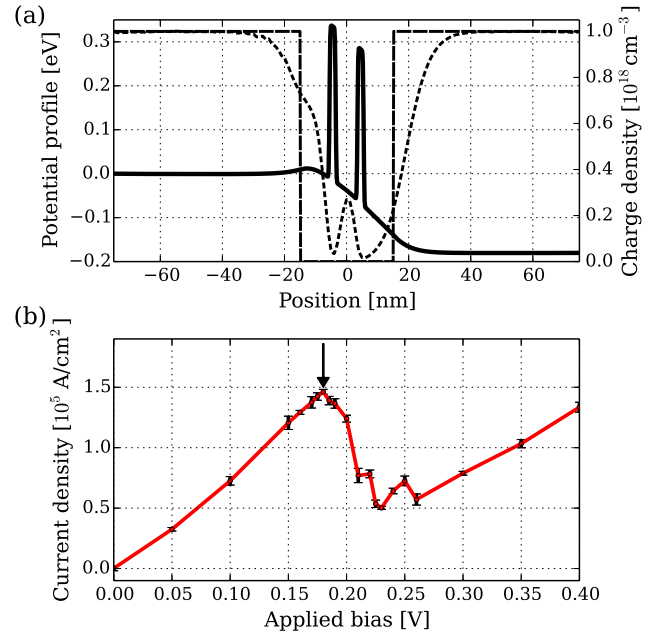

FIG. 4. (Color online) (a) Time-averaged potential profile (solid line) and charge density (short dashed line) as a function of position for the traditionally-doped RTD at an applied bias of 180 mV. Long dashed line shows the doping profile of the device. The potential profile is obtained from a self-consistent coupled solution of the WBTE and Poisson's equation. (b) Time-averaged current density vs applied bias. The time average is obtained over 1 ps intervals. The arrow marks the bias value 180 mV, which is used in (a).
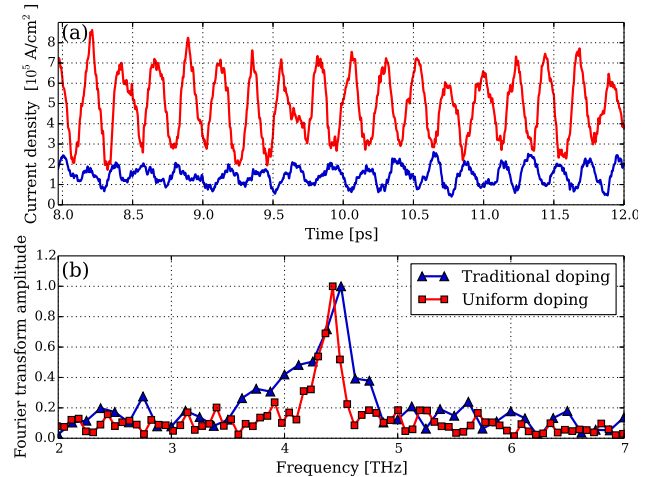

FIG. 5. (Color online) (a) Current density as a function of time for a bias of 180 mV (peak current) for the traditionally-doped RTD (lower blue curve) and a comparison with the uniformly-doped DBTS from Sec. III A for a bias of 0.096 mV (upper red curve). (b) Fourier spectrum of the current density oscillations for the traditionally-doped (blue curve) and uniformly-doped DBTS (red curve). Fourier transform amplitudes are normalized so the maximum equals one.

tent current oscillations for all values of bias, but only in

a limited bias window (175 mV to 185 mV) do the oscillations have a single well-pronounced Fourier component.

In Fig. 5, we observe intrinsic current oscillations when the traditionally-doped RTD is under peak bias of 180 mV. In Fig. 5a, we can see that the current density is smaller by a factor of ~ 3 compared with the uniformly-doped device at a bias of 96 mV. The amplitude of current oscillations (peak to bottom) is also smaller in the traditionally-doped case (1.5×10^5 A/cm^2 compared with 4.0×10^5 A/cm^2 in uniformly-doped device). As can be seen in Fig. 5b, due to the low current density in the traditionally-doped RTD, the main Fourier component of the current density is considerably widened by scattering, with respect to the uniformly-doped case.

C. Effects of scattering

In order to investigate the role of scattering, we ran simulations where the conventional scattering rates[22] were artificially modified via multiplication by a factor of 0.5 and 0.25. The results, as well as a comparison with the full scattering case (unchanged rates), are presented in Fig. 6, which shows the Fourier transform amplitude of the current density when the uniformly-doped DBTS from Sec. III A is biased in such a way that intrinsic oscillations are well resolved (96 mV).

With full scattering, the main frequency component has a full-width at half-maximum (FWHM) of 0.2 THz. Multiplying the scattering rates by a factor of 0.5 results in a reduced FWHM of about 0.08 THz. However, reducing the scattering rates further does not decrease the peak FWHM.
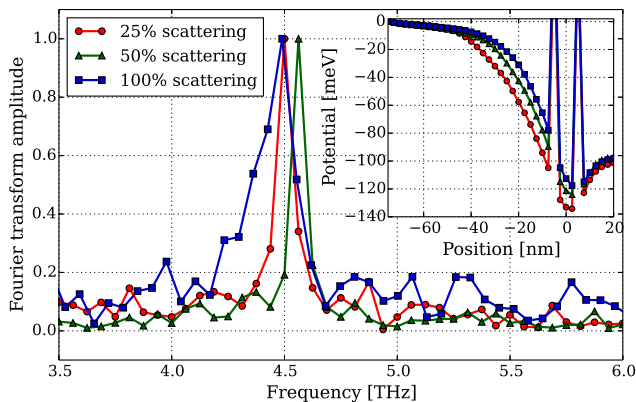

FIG. 6. (Color online) Fourier transform amplitude of the time-dependent current density for the uniformly-doped DBTS from Sec. III A with the full scattering rates (blue squares), 50% of the full scattering rates (green triangles) and 25% of the full scattering rates (red circles). The inset shows the corresponding time-averaged potential profiles for a part of the device.

D. The quasi-bound-state picture. The Coulomb mechanism behind the current-density oscillations

To get a qualitative picture of the mechanism behind the current oscillations, several authors have previously solved the time-independent Schrödinger equation (obtained eigenstates and energies) for a sub-region of the device in question[17,18,40]. Here, we do the same. The potential we use for the eigenvalue problem is the potential that was obtained by solving the coupled WBTE and Poisson's equation. Note that, due to the time-dependent distribution of charge in the device, the electrostatic potential is time-dependent. For a general time-dependent potential, solving the time-independent Schrödinger equation for different times is not meaningful. However, if the wave functions of the bound states vary weakly in time, an eigenvalue equation of the following form is valid[17]

$$\hat{H}(t)\psi_i(z,t) = E_i(t)\psi_i(z,t) \ , \qquad (8)$$

where $\hat{H}(t)$ is the system Hamiltonian, which includes the effects of the time-dependent "electrostatic" potential, ψ_i is the i-th eigenstate and $E_i(t)$ its corresponding energy.

Following such a procedure, we consider the emitter quantum well (EMQ) and main quantum well (MQW) regions of the uniformly-doped DBTS from Sec. III A *seperately* and solve the eigenvalue problem in each region (see Fig. 7a). This approach is only valid if the eigenfunctions are well-localized within each region. For example, in calculating the MQW bound states, we assume that the two barriers extend to $\pm\infty$ and use the boundary condition $\psi(\pm\infty) = 0$. A condition for the validity of the approach is that the resulting wavefunction does not penetrate deeper than 2 nm (the thickness of the barriers) into the barriers. From Fig. 7a, we can see that this is indeed the case — the well ground state does not extend into the emitter side and the emitter ground state does not penetrate into the well. Our motivation for the splitting of the emitter and well regions is to elucidate the nature of the temporal evolution of the device potential, shown in Fig. 8. We see that the largest Fourier components of potential oscillations in both the EQW and MQW regions are at frequencies around 9.6 THz, considerably higher than the frequency of current oscillations (4.5 THz). We note that the high-frequency oscillations correspond to the bulk electron plasma frequency in GaAs, given by

$$f_p = \frac{1}{2\pi}\sqrt{\frac{nq^2}{\varepsilon m^*}} \simeq 9.65 \text{ THz} \ , \qquad (9)$$

with an electron density equal to the doping density $n = 10^{18}$ cm^{-3} and $\varepsilon = 12.8\varepsilon_0$ the dielectric constant of GaAs. However, the high-frequency potential oscillations of the two wells are in phase; in contrast, the potential difference between the two regions oscillates with the same frequency as the current, implying that the current
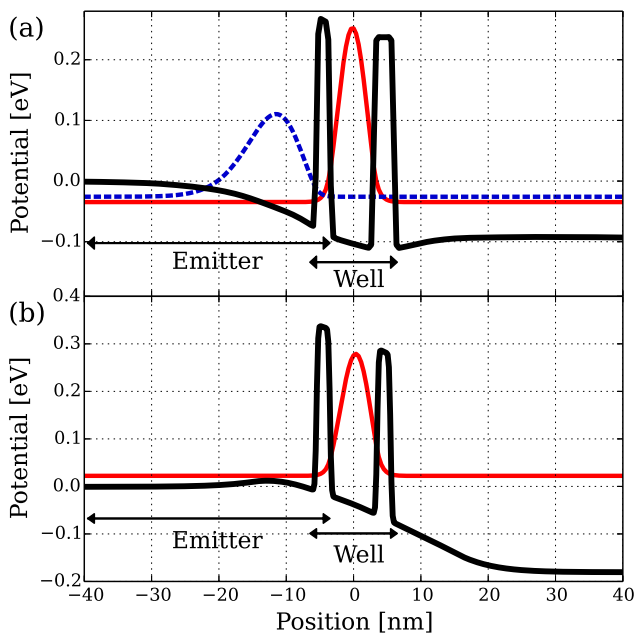
FIG. 7. (Color online) (a) Snapshot of the potential pro-
file (thick black curve) for the uniformly-doped DBTS from
Sec. III A at an applied bias of 96 mV (bias for which intrinsic
oscillations are observed). The solid red and the dashed blue
curves correspond to the ground state probability densities in
the well and emitter regions, respectively. (b) Snapshot of
potential profile (thick black curve) of the traditionally-doped
RTD from Sec. III B in a steady state for an applied bias of
180 mV (bias for which intrinsic oscillations are observed).
The solid red curve corresponds to the ground state proba-
bility density of the main quantum well bound state. The
emitter quantum well is very shallow and contains no bound
states. In both (a) and (b), the two arrows define the emit-
ter and well regions (the computational domain for the wave
functions). The two domains overlap in the region of the left
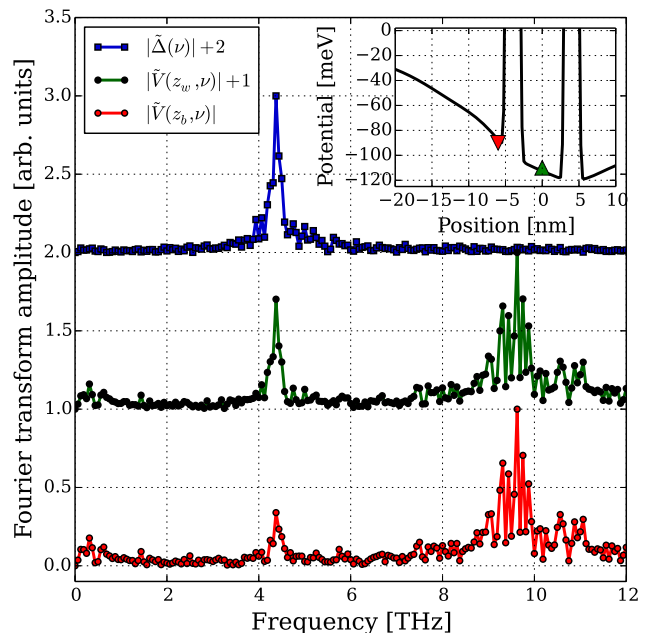barrier.

FIG. 8. (Color online) Fourier transforms of the potential on
the left side of the first barrier at $z_b = 6$ nm (red open cir-
cles), the middle of the well at $z_w = 0$ (green closed circles)
and the potential difference $\Delta(t) = V(z_b,t) - V(z_w,t)$ (blue
squares) for the uniformly-doped DBTS from Sec. III A. In
the legend, the tilde denotes a Fourier transform from the
time to frequency (ν) domain. The inset shows a snapshot of
the potential profile where the positions z_b (red downward-
pointing triangle) and z_w (green upward-pointing triangle)
are marked. The figure shows that the largest Fourier com-
ponents of the emitter and well potential oscillations are for
frequencies above the intrinsic current oscillations. However,
these high-frequency plasmonic oscillations [Eq. (9)] are in
phase, as are the low frequency oscillations around 0.4 THz.
In contrast, the potential difference between the barrier and
well region oscillates with the same frequency as the current
density (4.5 THz).

oscillations are Coulombic in nature and that the electro-
static potential difference between the two regions plays
a central role in the mechanism. The Coulomb nature of
the mechanism was qualitatively mentioned in[41] in con-
nection with a simplified 1D version of the DBTS, fea-
turing a linear potential drop across the well and barriers
and a constant density of states in the contacts. However,
we found that the oscillations were impossible to observe
with a linear potential drop; a self-consistent solution of
coupled Poisson's equation and a transport kernel is nec-
essary to capture the oscillations. In fact, current oscilla-
tions in the DBTS appear to be closely related to the ex-
perimentally observed phenomena of charge bistability[42]
and self-sustained oscillations in doped superlattices[43,44],
which are associated with the formation of electric-field
domains[45]. The doped DBTS might be considered as the
ultra-short limit of a doped superlattice, which also im-
plies a higher frequency of oscillations (THz in the DBTS,
as opposed to the MHz – GHz frequency range observed
in superlattices[44]).

Figure 9a shows the results of the same bound state
analysis as in Fig. 7a, performed at different times over
a time period of 4 ps. The figure shows that the energy
difference between the ground states in the EQW and
MQW, defined by $\Delta(t) = E_{MQW}(t) - E_{EQW}(t)$, is os-
cillating with the same frequency as the current density
oscillations (also plotted in Fig. 9) with a minimum near
zero. With increased current, charge accumulates in the
MQW, raising the energy of the MQW state out of align-
ment with the EQW state via the self-consistent electro-
static potential. Charge then tunnels from the MQW
region into the collector, lowering the well bound state
back into alignment with the emitter state. The process
is cyclic and is the cause of the periodic current oscilla-
tions.

There is a phase difference of about 49° between the
peak in the current density and Δ. The current actually
takes the highest value when the MQW energy is slightly
(by about $10\,\text{meV} \approx k_B T/2$) higher than the EQW en-

ergy. The phase difference has to do with considerable inelastic scattering and the fact that the system is non-degenerately doped, with the Fermi level below the conduction band edge; the states are populated according to the distribution-function tail, so the concept of level alignment holds with an energy uncertainty on the order of $k_B T/2$.

Figure 9b shows that temporal variation in the EQW ground state wavefunction is small and time variation of the MQW state (not shown) would not be visible on a similar graph, justifying our use of Eq. (8). The reason the wave functions are only weakly affected is that most of the time-dependent potential drop between the bottom of the EQW and the center of the MQW takes place inside the left barrier, where the EQW and MQW ground states have very small amplitudes and are therefore only weakly affected.

In the case of the traditionally-doped RTD from Sec. III B, the EQW is too shallow to form a bound state (see Fig. 7b). However, as already mentioned in Sec. III B, we still observe intrinsic current oscillations when the RTD is biased in such a way that it exhibits peak current (resonant condition). As can be seen in Fig. 7b, under these resonant conditions, the MQW quasi-bound ground state is slightly (on the order of $k_B T$) higher than the emitter conduction band edge and a large portion of incoming electrons have energy matching the MQW ground state and current is at a maximum. With increased current, the amount of charge in the well goes up, bringing the MQW state out of the transport window via the self consistent electrostatic potential. As in the case for the uniformly-doped DBTS, the process is cyclic and is the cause for the intrinsic current oscillations.

E. Frequency of the current-density oscillations. Effect of varying doping density

In a model proposed by Zhao *et al.* [17], the frequency of intrinsic current oscillations is given by $\tilde{\Delta}/h$, where $\tilde{\Delta}$ is the time average of $\Delta(t)$. From the data presented in Fig. 9a, we get $\tilde{\Delta}/h \simeq 1.7$ THz, which is well below 4.5 THz, the frequency of the current density oscillations (Fig. 8). Another important difference between our results and the results of Zhao *et al.* is that they found the potential oscillations in the EQW and MQW to be completely in-phase, and thus concluded that the current oscillations were not driven by the charge exchange between the EQW and MQW, i.e., that the source of current oscillations is not the long-range Coulomb interaction. In contrast, as shown earlier in this section, we found that current oscillations are driven by the time-dependent potential difference between the EQW and MQW. Sakurai and Tanimura worked within a hierarchy-equation-of-motion formalism and also observed intrinsic current oscillations in RTDs [18,19]. To explain their results, they performed a similar bound-state analysis. However, for
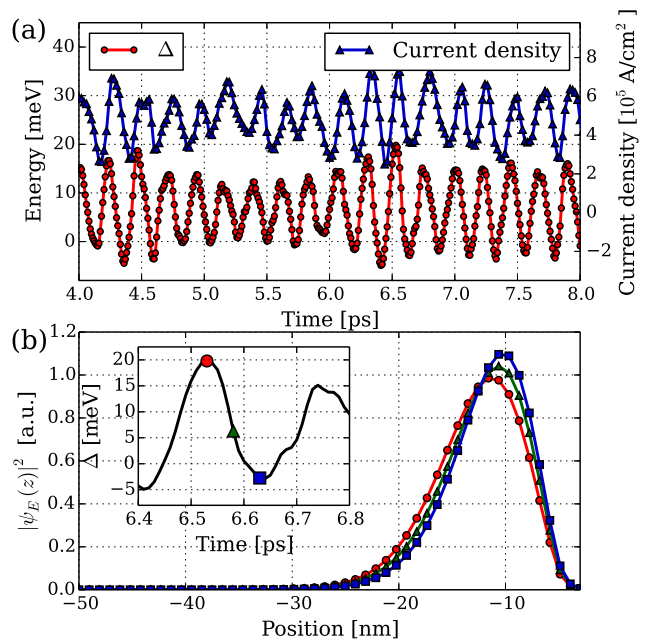

FIG. 9. (Color online) (a) Time evolution of Δ, the energy difference between the MQW ground state and the EQW ground state (red circles) and current density (blue triangles) for the uniformly-doped DBTS from Sec. III A. From the figure we see that the energy difference between the ground states in the EQW and the MQW is oscillating with the same frequency as the current density and is close to zero when Δ is at a minimum. The current density leads Δ in phase by 49°. (b) Probability density for the emitter ground state at a few points in time (the corresponding values of Δ are denoted in the inset). We see that the EQW wavefunction varies weakly over time.

their eigenvalue problem, they used a time average of the device potential. When we employed the method proposed by Sakurai and Tanimura, we were not able to predict the frequency of current oscillations. This result is not surprising, considering that, in time-averaging the device potential, we lose all information about the potential variation between the EQW and MQW, which plays a pivotal role in the current oscillations in the present work. On the other hand, Ricco and Azbel[41], who qualitatively discussed the Coulomb origin of the oscillations, argued that the oscillation frequency would be on the order of the carrier lifetime in the well, related to the peak width in the coherent transmission coefficient.

Here, we show that the frequency of current oscillations is in fact determined by the ratio of charges stored in the MQW and EQW, and that it can be tuned by varying the doping density. We observe well-resolved (near single-frequency) intrinsic current oscillations in the uniformly-doped DBTS presented in Sec. III A for doping density in the range $0.8 - 1.8 \times 10^{18}$ cm^{-3}, where frequency can be tuned between 4.2 THz and 4.9 THz (see Fig. 10a). Figure 10 shows how several physical quantities vary with doping density. From Fig. 10a we see that the frequency of oscillation is a non-monotonically increasing function

of doping density. The amplitude of current oscillation J_A (Fig. 10b) has a maximum between 1.5×10^{18} cm^{-3} and 1.7×10^{18} cm^{-3} and from Fig. 10c we see that the relative current-oscillation amplitude J_A/J_{av} (J_{av} is the time-averaged current density) varies weakly once doping is increased above 1.0×10^{18} cm^{-3}. Below doping of 1.0×10^{18} cm^{-3}, the relative current-oscillation amplitude decreases rapidly with decreasing doping density. Modifying the doping density affects the IV-diagram of the device and shifts the operating bias. By operating bias, we mean the bias in which the device exhibits the clearest current oscillations (lowest FWHM of the main Fourier transform amplitude). Figure 10d shows how the operating bias changes with doping density. Figure 10e shows that the frequency of current oscillations is roughly a linear function of the ratio Q_{MQW}/Q_{EQW}, where Q_{MQW} is the time-averaged total charge (per unit area) in the MQW region and Q_{EQW} is the time-averaged total charge in the EQW region. In calculating Q_{EQW}, we intergrate the charge density over a region extending 20 nm to the left of the left barrier, corresponding roughly to the extent of the EQW shown in Fig. 7a.

Outside of the doping range $0.8 - 1.8 \times 10^{18}$ cm^{-3}, current still oscillates, but with a much greater frequency spread, similar to the top and bottom panels in Fig. 3. When scattering rates are artificially lowered, we observe the intrinsic current oscillations for doping densities lower than 0.8×10^{18} cm^{-3}, so we conclude that for doping densities lower than 0.8×10^{18} cm^{-3}, the long-range Coulomb force cannot sustain periodic current oscillations owing to the dampening effects from phonon and ion scattering. As the doping density is increased, the potential well on the collector side of a uniformly-doped DBTS gets deeper and a large amount of charge builds up in this well (see Fig. 11). We suspect that the charge exchange between the collector well and the main quantum well is what disturbs intrinsic current oscillations for higher doping densities. To prevent the collector quantum well from forming, other doping profiles can be considered, such as a gradual doping density towards the collector side. Another possible explanation for the lack of well-resolved intrinsic current oscillations at higher doping densities is that, as the doping density is increased, potential variations due to the electron plasma oscillations are stronger (have a larger Fourier amplitude) and a higher frequency (see Fig. 12), and the quasistatic picture presented in Sec. III D may not be warranted.

F. Experimental Considerations Relevant for Observing Persistent Oscillations

Since the well-resolved current oscillations are only observed when the ground states in the EQW and MQW have similar energies, it is expected that they will be notable only in a limited bias window in which this alignment takes place. For the 6-nm-well uniformly-doped DBTS, this range is 94–98 mV (Fig. 2); below 94 mV,
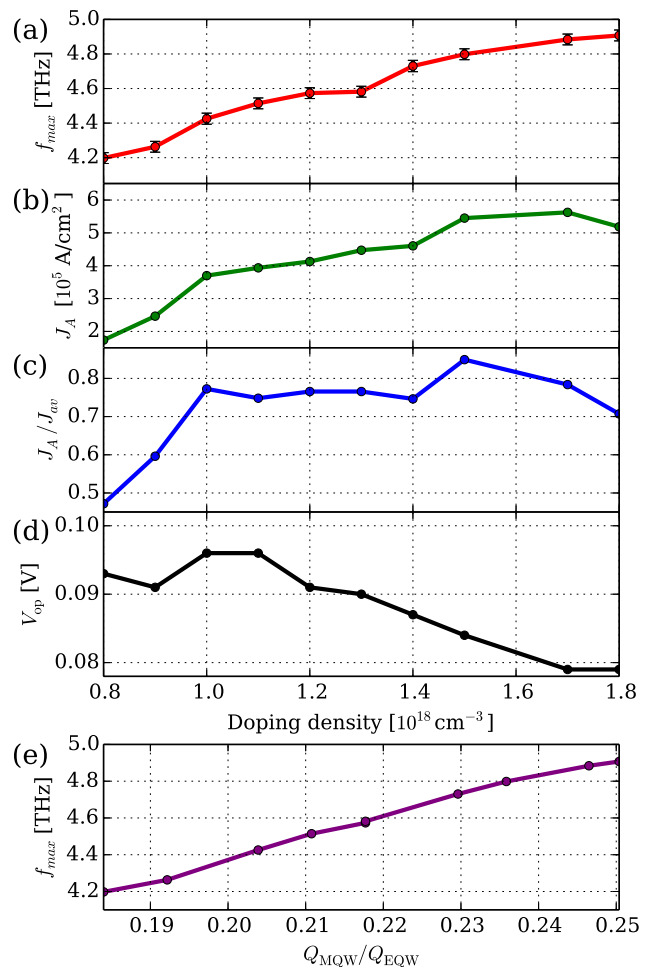

FIG. 10. (Color online) (a) Frequency of current oscillation f_{max} vs doping density. (b) Amplitude of current oscillations J_A vs doping density. The amplitude is calculated using $J_A = 2\sqrt{2}\sigma$, where σ is the standard deviation in current density. (c) Relative amplitude of current oscillations J_A/J_{av} where J_{av} is the time averaged current density. (d) Operating bias V_{op} (see main text for definition) as a function of doping density. (e) Frequency of current oscillations vs the ratio of time averaged charge in the MQW and the EQW (see main text for details). All panels are for the uniformly-doped DBTS from Sec. III A.

the MQW ground state is considerably above the EQW one, while above 98 mV the order reverses.

The necessity of this alignment is manifested in the sensitivity of the oscillation prominence on the DBTS geometry. While the 6-nm-well uniformly-doped DBTS supports really sharp-frequency, large-amplitude oscillations, a similar 7-nm-well uniformly-doped DBTS (Fig. 2) does not. The reason is the strong dependence of the MQW ground state energy on the well width, where a wider well translates into a lower ground state energy. A natural follow-up question is why the current oscillations are simply not observed at a lower bias, but at a low bias the EQW is too shallow to support a well-localized
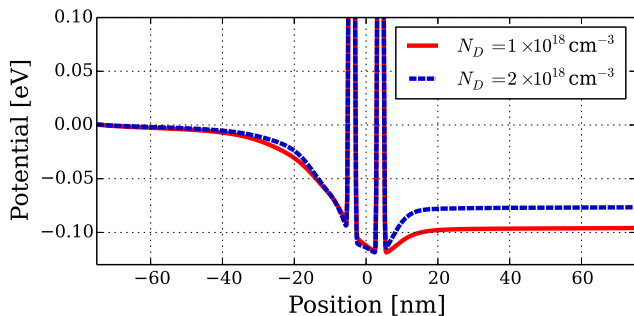
FIG. 11. (Color online) Time-averaged potential profile in the uniformly-doped DBTS from Sec. III A at a doping density of 1.0×10^{18} cm^{-3} (solid red) and 2.0×10^{18} cm^{-3} (dashed blue) for applied bias of 96 mV and 77 mV, respectively. For the higher doping density, the potential well on the collector side is deep enough to form a bound state, which disrupts the current density oscillations that are governed by charge transfer between the emitter and main quantum wells.
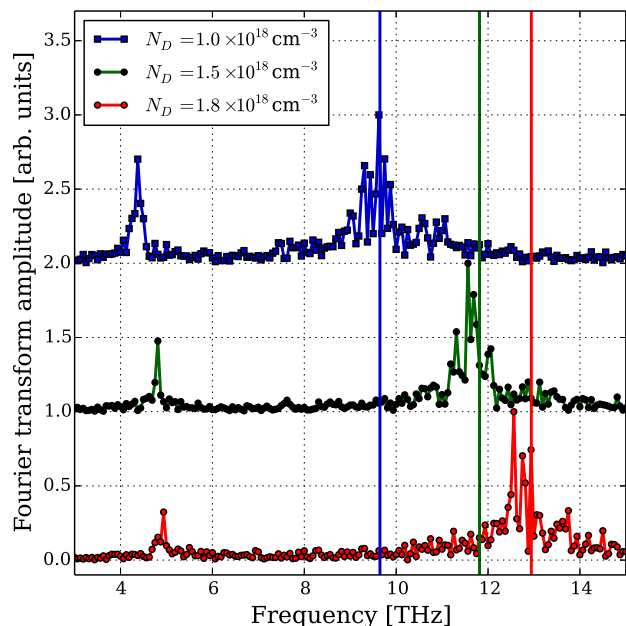

FIG. 12. (Color online) Fourier transform of the time-dependent potential value at the center of the MQW region, corresponding to $V(z_w, t)$ in Fig. 8, for doping densities of 1.0×10^{18} cm^{-3} (blue squares), 1.5×10^{18} cm^{-3} (filled circles) and 1.8×10^{18} cm^{-3} (red circles). Vertical lines mark the corresponding electron plasma frequencies, 9.65 THz, 11.81 THz, and 12.94 THz, respectively. Plasma frequences are calculated using Eq. (9), assuming an electron density equal to doping density. We see that, as the electron density is increased, plasma oscillations increase both in frequency and amplitude. The lower-frequency Fourier component, corresponding to the frequency of intrinsic current oscillations, varies more slowly and remains between 4 and 5 THz.

bound state. Current oscillations are thus very sensitive to quantum-well-width fluctuations. As the lattice parameter for GaAs is about 0.5 nm, monolayer precision

is fabrication in required to observe the oscillations.

Barrier thickness is another parameter that can fluctuate in fabricated devices. We performed simulations for uniformly-doped DBTSs with the same well width (6 nm) but with thicker (3 nm) and thinner (1 nm) barriers than the 2-nm one, which had been found as ideal for the minimal frequency spread and highest amplitude. We found that varying the barrier thickness had a negligible effect on the frequency of current oscillations. The main effect of the increased barrier width was a drastic decrease in the amplitude of both current oscillations and the time-averaged current, because thicker barrier impede tunneling. The effect of barrier thinning washed out the oscillations, because with very thin wells the EQW and MQW states cease to be well-localized in their respective wells (Sec. III D). Consequently, the barrier thickness also has to be achieved with monolayer precision.

The doping density is a parameter that critically affects the characteristic frequency of intrinsic current oscillations. As the current oscillations are driven by a cyclic redistribution of charge in the device, the frequency will be on the same order of magnitude as the 3D plasma frequency for the electron density equal to the doping density, Eq. (9). An accurate prediction of the frequency, however, requires a detailed numerical calculation.

IV. SUMMARY AND CONCLUDING REMARKS

By solving the WBTE self-consistently coupled with Poisson's equation, we analyzed the persistent THz current oscillations in GaAs/AlGaAs-based DBTSs. We showed that a uniform doping profile results in a higher amplitude of current oscillations, as well as a reduced frequency spread, than the traditional doping profiles, where the well region is undoped. By varying device parameters, we found that the barrier and well widths of 2 nm and 6 nm, respectively, provided the greatest amplitude of current oscillations as well as the lowest frequency spread (FWHM of the main Fourier component). We provided a qualitative explanation for the source of current oscillations by employing a quasistatic picture, where localized states in the EQW and MQW are periodically tuned in and out of alignment due to a redistribution of charge between the EQW and MQW. The frequency of current oscillations was found to depend linearly on the ratio of the time average of the charge stored in the EQW and MQW regions. We found that the frequency of current oscillations in a uniformly-doped DBTS can be tuned by varying the doping density between 0.8×10^{18} cm^{-3} and 1.8×10^{18} cm^{-3}. In this doping range, frequency is a nonmonotonically increasing function of doping density and can be varied between 4.2 and 4.9 THz, with a typical frequency spread of 0.2 THz. The highest amplitude of current oscillations we observed was 5.5×10^5 A/cm^2, for a doping density in the range 1.5 to 1.7×10^{18} cm^{-3}. However, above the doping den-

sity of 1.0×10^{18} cm^{-3}, the ratio of the current-density-oscillation amplitude and the average current density did not vary considerably and had values in the range 0.7 to 0.8.

We conclude that utilization of intrinsic current oscillations in uniformly-doped DBTSs shows potential for solid-state-based ac-current generation in the THz range at room temperature. However, as we have demonstrated, tunability of the frequency of oscillation is limited (4.2 to 4.9 THz). The limited tuning range is a consequence of the fact that the ratio of time-averaged charge in the EQM and MQW does not vary considerably in the doping range in which intrinsic current oscillations are manifested. In order to provide more tunability, it is worth considering the effect of a more complicated doping profile and variation of other device parameters. Another limitation is the ~ 0.2 THz frequency spread of the main Fourier component of current oscillations. We showed that artificially reducing scattering rates reduces the frequency spread and allows us to observe well-resolved intrinsic current oscillations at lower doping densities. Experimentally, lowering the scattering rates can be accomplished by lowering the temperature and doping density. However, tuning the temperature also changes the distribution of electrons in the contacts and modification of the doping profile results in changes in the electrostatic potential. Optimization of the RTD performance as a THz power source with respect to temperature and doping profile is therefore an involved process and is beyond the scope of this publication. Another possible extension to the current work is a self-consistent solution of the WBTE with Maxwell's equations, to estimate the radiated power and account for losses due to attenuation. Last but not least, the effect of nonequilibrium phonons and lattice heating on intrinsic oscillations in DBTSs is an interesting open question.

Appendix: Bias Treatment

The method we use to solve the WBTE in Eq. (1) requires use to perform a Wigner transform of the fast varying-potential term V_{qm} defined in Eq. (3). A more computationally efficient way is to use[46]

$$V_w(z,k) = \frac{2}{\pi\hbar}\mathrm{Im}\left\{e^{2ikz}\tilde{V}_{\mathrm{qm}}(2k)\right\} \;, \qquad (A.1)$$

where $\tilde{V}_{\mathrm{qm}}(k,t)$ is the spatial Fourier transform of $V_{\mathrm{qm}}(z,t)$ with the convention

$$\tilde{V}_{\mathrm{qm}}(k,t) = \int\limits_{-\infty}^{\infty} V_{\mathrm{qm}}(z,t)e^{-ikz}\mathrm{d}z \;. \qquad (A.2)$$

Equation (A.2) represents a problem when V_{qm} does not decay to zero as $z \to \pm\infty$, such in the case of an applied bias. As an example, let us take a prototype bias potential of the form (erf is the error function)

$$V_\Delta(z) = -\frac{V_0}{2}\,\mathrm{erf}[\beta(z-z_0)] \;, \qquad (A.3)$$

which represents a bias drop of V_0, antisymmetric around z_0 and β controls how abruptly the potential changes (see Fig. 13). Because V_Δ does not decay to zero as $z \to \pm\infty$, its Fourier transform is only defined in the distributional sense which makes a numerical evaluation troublesome. However, the Wigner transform of V_Δ can be done analytically using Eq. (A.2), giving

$$V_{w,\Delta}(z,k) = \frac{V_0}{\hbar\pi}\mathcal{P}\frac{1}{k}e^{-k^2/\beta^2}\cos[2k(z-z_0)] \;, \qquad (A.4)$$

where $\mathcal{P}$ denotes the principal value. The quantum evolution term resulting from $V_{w,\Delta}$ can be calculated using Eq. (2), giving

$$\begin{aligned}
Q_{V_\Delta}[f_w](z,k) &= \int\limits_{-\infty}^{\infty} V_{w,\Delta}(z,k')f_w(z,k-k')\mathrm{d}k' \\
&= \frac{V_0}{\pi\hbar}\int\limits_{-\infty}^{\infty}\mathcal{P}\frac{1}{k'}e^{-k'^2/\beta^2}\cos[2k'(z-z_0)]f_w(z,k-k')\mathrm{d}k' \\
&= \frac{V_0}{\pi\hbar}\int\limits_{-k_c}^{k_c}\mathcal{P}\frac{1}{k'}e^{-k'^2/\beta^2}\cos[2k'(z-z_0)]f_w(z,k-k')\mathrm{d}k' \\
&\quad + \frac{V_0}{\pi\hbar}\int_{|k'|>k_c}\mathcal{P}\frac{1}{k'}e^{-k'^2/\beta^2}\cos[2k'(z-z_0)]f_w(z,k-k')\mathrm{d}k' \\
&\equiv Q_{V_\Delta,c} + Q_{V_\Delta,\infty}
\end{aligned} \qquad (A.5)$$

where $k_c > 0$ is a cutoff wave number. In Eq. (A.5), we have split the k' integral into the long wavelength part $Q_{V_\Delta,c}$ and short wavelength part $Q_{V_\Delta,\infty}$. If we choose k_c small enough such that $f_w(z,k)$ varies weakly in the range $[k-k_c,k+k_c]$, we can replace $f_w(z,k)$ with its first

order Taylor expansion in the neighborhood of k and get

$$Q_{V_\Delta,c}[f_w] = -\frac{V_0}{\pi\hbar}\frac{\partial f_w}{\partial k}\int_{-k_c}^{k_c} e^{-k'^2/\beta^2}\cos[2k'(z-z_0)]\mathrm{d}k'$$

$$= -\frac{1}{\hbar}\frac{\partial f_w}{\partial k}\frac{\beta V_0}{\sqrt{\pi}}e^{(z-z_0)^2\beta^2}\,\mathrm{Re}\left\{\mathrm{erf}[k_c/\beta + i(z-z_0)\beta]\right\}$$

$$\equiv -\frac{1}{\hbar}\frac{\partial f_w}{\partial k}F_\Delta(z)\;. \tag{A.6}$$

where Re refers to the real part. Comparison with Eq. (1) shows that the quantum evolution term in Eq. (A.6) has reduced to a semi-classical drift term with force F_Δ defined in the bottom line of Eq. (A.6) and can be absorbed into the slowly varying potential term such that $F_\Delta(z) = -\partial V_{\mathrm{cl}}/\partial z$. The short wavelength part $Q_{V_\Delta,\infty}$ is still treated quantum mechanically. When choosing a length for the considered device, care must be taken that the device is long enough such that $F_\Delta(z)$ is small outside the device region.

Now consider the potential profile of the uniformly-doped DBTS from section III A under an applied bias of 0.096 V (see Fig. 13). Define the total potential as $V(z)$. Now define a new quantity

$$V_\delta(z) = V(z) - V_\Delta(z) - V_B(z)\;, \tag{A.7}$$

where $V_B(z)$ is the potential of the barriers. Figure 13 shows a plot of $V_\delta(z)$. The main idea is to compute the Wigner transform of V_B and V_Δ analytically, so that only the Wigner transform of V_δ needs to be performed numerically. Any numerical difficulties are avoided because V_δ varies slowly and decays rapidly to zero for $z \to \pm\infty$, due to the fact that we have removed the barriers through V_B and the potential drop through V_Δ.

Analytic evaluation of the Wigner transform of a barrier potential can be done by considering it as a linear combination of error functions. For example the potential of the left barrier can be written as

$$V_{LB}(z) = \frac{V_L}{2}\{-\mathrm{erf}[\beta_L(z - z_L - a_L)]$$
$$+ \mathrm{erf}[\beta_L(z - z_L + a_L)]\}\;, \tag{A.8}$$

where the subscript L refers to the left potential barrier, $2a_L$ is the barrier width, V_L the barrier height, z_L its center position and β_L controls how much the barrier edge is smoothed. The barrier becomes abrupt in the limit $\beta_L \to \infty$, however a finite value must be used because the numerical method we use is only convergent for continuous potentials[47]. The corresponding Wigner transform is

$$V_{w,LB}(z,k) = \frac{2V_L}{\hbar\pi}\frac{1}{k}e^{-k^2/\beta_L^2}\sin[2k(z-z_L)]\sin[2ka_L]\;. \tag{A.9}$$

We note that this approach does not only work for RTDs, but any device with an applied potential where computation of the Wigner potential is required. The specific choice of parameters β and z_0 in the bias potential is not important, however, a good guess will minimize V_δ, which contains the part of the total potential which must be Wigner transformed numerically.
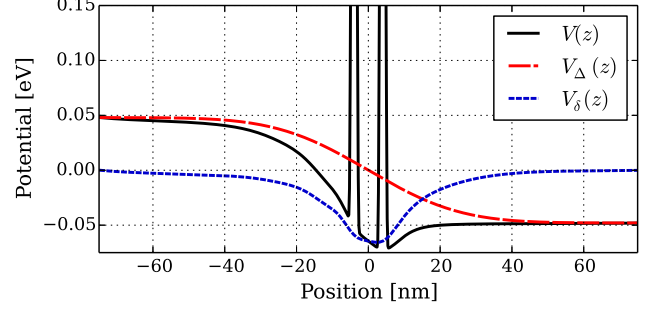

FIG. 13. (Color online)Solid black curve shows the potential profile for the uniformly-doped DBTS described in Sec. III A. Long-dashed red curve shows the bias potential $V_\Delta(z)$, with parameters $\beta = 0.035$ nm^{-1}, $z_0 = 0$, and $V_0 = 0.096$ eV. Short-dashed blue curve shows $V_\delta(z)$, which is the potential remaining when the bias and barriers have been subtracted from the total potential $V(z)$.

* ojonasson@wisc.edu

† knezevic@engr.wisc.edu

[1] M. Tonouchi, Nature Photon. **1**, 97 (2007).

[2] D. M. Mittleman, J. Cunningham, M. Nuss, and M. Geva, Appl. Phys. Lett. **71**, 16 (1997).

[3] D. Hashimshony, I. Geltner, G. Cohen, Y. Avitzour, A. Zigler, and C. Smith, J. Appl. Phys. **90**, 5778 (2001).

[4] A. Dobroiu, M. Yamashita, Y. N. Ohshima, Y. Morita, C. Otani, and K. Kawase, Appl. Opt. **43**, 5637 (2004).

[5] K. Kawase, Y. Ogawa, Y. Watanabe, and H. Inoue, Opt. Express **11**, 2549 (2003).

[6] J. H. Booske, Phys. Plasmas **15**, 055502 (2008).

[7] T. C. L. G. Sollner, E. R. Brown, W. D. Goodhue, and H. Q. Le, Appl. Phys. Lett. **50**, 332 (1987).

[8] N. Orihashi, S. Suzuki, and M. Asada, Appl. Phys. Lett. **87**, 233501 (2005).

[9] S. Suzuki, M. Asada, A. Teranishi, H. Sugiyama, and H. Yokoyama, Appl. Phys. Lett. **97**, 242102 (2010).

[10] M. Feiginov, C. Sydlo, O. Cojocari, and P. Meissner, Appl. Phys. Lett. **99**, 233506 (2011).

[11] H. Kanaya, S. Suzuki, and M. Asada, IEICE Electron. Express **10**, 20130501 (2013).

[12] D. L. Woolard, E. R. Brown, F. A. Buo, X. J. Lu, D. L. Rhodes, and B. S. Perlman, in *Device Research Conference, 1995. Digest. 1995 53rd Annual* (1995).

[13] K. L. Jensen and F. A. Buo, Phys. Rev. Lett. **66**, 1078 (1991).

[14] B. A. Biegel and J. D. Plummer, Phys. Rev. B **54**, 8070 (1996).

[15] Z. Dai and J. Ni, Phys. Rev. B **73**, 113309 (2006).

[16] P. Wojcik, J. Adamowski, M. Wołoszyn, and B. J. Spisak, Phys. Rev. B **86**, 165318 (2012).

[17] P. Zhao, D. L. Woolard, and H. L. Cui, Phys. Rev. B **67**, 085312 (2003).

[18] A. Sakurai and Y. Tanimura, New J. Phys. **16**, 015002 (2014).

[19] A. Sakurai and Y. Tanimura, J. Phys. Soc. Jpn. **82**, 033707 (2013).

[20] L. Shifren and D. Ferry, Phys. Lett. A **285**, 217 (2001).

[21] D. Querlioz and P. Dollfus, *The Wigner Monte-Carlo Method for Nanoelectronic Devices: A Particle Description of Quantum Transport and Decoherence* (Wiley, 2013).

[22] M. Lundstrom, *Fundamentals of carrier transport*, 2nd ed. (Cambridge University Press, 2000).

[23] P. Wojcik, B. J. Spisak, M. Woloszyn, and J. Adamowski, J. Appl. Phys. **111**, 124310 (2012).

[24] L. Shifren and D. Ferry, Physica B **314**, 72 (2002), proceedings of the Twelfth International Conference on Nonequilibrium Carrier Dynamics in Semiconductors.

[25] W. R. Frensley, Rev. Mod. Phys. **62**, 745 (1990).

[26] C. Jacoboni, R. Brunetti, P. Bordone, and A. Bertoni, Int. J. Hi. Spe. Ele. Syst. **11**, 387 (2001).

[27] E. Wigner, Phys. Rev. **40**, 749 (1932).

[28] D. K. Ferry, *Semiconductors* (IOP Publishing, 2013).

[29] P. Wojcik, B. Spisak, M. Woloszyn, and J. Adamowski, Acta Phys. Pol., A **114**, 1431 (2008).

[30] D. Querlioz, H.-N. Nguyen, J. Saint-Martin, A. Bournel, S. Galdin-Retailleau, and P. Dollfus, J. Comput. Electron. **8**, 324 (2009).

[31] M. Nedjalkov, H. Kosina, S. Selberherr, C. Ringhofer, and D. K. Ferry, Phys. Rev. B **70**, 115319 (2004).

[32] M. Nedjalkov, P. Schwaha, S. Selberherr, J. M. Sellier, and D. Vasileska, Appl. Phys. Lett. **102**, 163113 (2013).

[33] M. Nedjalkov, S. Selberherr, , and I. Dimov, "Numerical methods and applications," (Springer, Berlin Heidelberg, 2011) pp. 95–102.

[34] L. Shifren, C. Ringhofer, and D. K. Ferry, IEEE Trans. Electron Dev. **50**, 769 (2003).

[35] W. Shockley, Journal of Applied Physics **9**, 635 (1938).

[36] S. Ramo, Proceedings of the IRE **27**, 584 (1939).

[37] D. Querlioz, J. Saint-Martin, and P. Dollfus, J. Comput. Electron. **9**, 224 (2010).

[38] D. Vasileska, K. Raleeva, S. M. Goodnick, C. Ringhofer, S. S. Ahmed, N. Ashraf, A. Hossain, R. Hathwar, A. Ashok, and B. Padmanabhan, "Monte carlo device simulations," (http://www.nanohub.org/resources/10579/download) Chap. Nanohub Resources on Monte Carlo Device Simulations Study, pp. 1–76.

[39] H. Kressel and J. K. Butler, *Semiconductor Lasers and Herterojunction LEDs* (Academic Pr, 1977).

[40] P. Wojcik, B. J. Spisak, M. Woloszyn, and J. Adamowski, Semicond. Sci. Technol. **25**, 12 (2010).

[41] B. Ricco and M. Y. Azbel, Phys. Rev. B **29**, 1970 (1984).

[42] Y. Zhang, R. Klann, K. H. Ploog, and H. T. Grahn, Appl. Phys. Lett. **70** (1997).

[43] J. Kastrup, R. Klann, H. T. Grahn, K. Ploog, L. L. Bonilla, J. Galán, M. Kindelan, M. Moscoso, and R. Merlin, Phys. Rev. B **52**, 13761 (1995).

[44] J. Kastrup, R. Hey, K. H. Ploog, H. T. Grahn, L. L. Bonilla, M. Kindelan, M. Moscoso, A. Wacker, and J. Galán, Phys. Rev. B **55**, 2476 (1997).

[45] A. Wacker, Physics Reports **357**, 1 (2002).

[46] M. Nedjalkov, H. Kosina, and P. Schwaha, J. Comput. Electron. **9**, 218 (2010).

[47] A. Arnold and F. Nier, Math. Comp. **58**, 645 (1992).